Novel three-dimensionally ordered macroporous SrTiO$_3$ photocatalysts with remarkably enhanced hydrogen production performance

Kai Yu [a,b,*], Chenxi Zhang [b,c], Yue Chang [b,c], Yajun Feng [a], Zequn Yang [a], Ting Yang [b,c], Lan-Lan Lou [b,c], Shuangxi Liu [b,c,d,**]

[a] MOE Key Laboratory of Pollution Processes and Environmental Criteria, College of Environmental Science and Engineering, Nankai University, Tianjin 300350, People's Republic of China
[b] Institute of New Catalytic Materials Science, School of Materials Science and Engineering, Nankai University, Tianjin 300350, People's Republic of China
[c] National Institute of Advanced Materials, Nankai University, Tianjin 300350, People's Republic of China
[d] Collaborative Innovation Center of Chemical Science and Engineering (Tianjin), Tianjin 300072, People's Republic of China

ARTICLE INFO

ABSTRACT

Three-dimensionally ordered macroporous SrTiO$_3$ (3DOM-SrTiO$_3$) materials with different pore sizes were originally prepared and employed as photocatalysts in the water splitting for hydrogen generation. These 3DOM-SrTiO$_3$ photocatalysts were characterized by XRD, SEM, TEM, EDS, DR UV–vis and N$_2$ sorption. Because of the slow photon effect of 3DOM-SrTiO$_3$, notably enhanced efficiency of water splitting for hydrogen evolution was obtained compared with the solid-state SrTiO$_3$ (SS-SrTiO$_3$) and disordered porous SrTiO$_3$ (Disorder-SrTiO$_3$). The effect of stop-band on the efficiency of photocatalytic hydrogen production was studied by tuning the pore diameter of 3DOM-SrTiO$_3$. It was found that higher hydrogen evolution efficiency could be achieved when the photonic stop-band of 3DOM-SrTiO$_3$ was overlapped with its band gap, which was further confirmed by the control experiments under certain wavelength light irradiation. 3DOM-SrTiO$_3$(270 nm) exhibited the highest photocatalytic hydrogen evolution rate (up to 3599 μmol/g·h), which was 31 times as high as that of SS-SrTiO$_3$ and 11 times higher than that of Disorder-SrTiO$_3$. Furthermore, these 3DOM-SrTiO$_3$ catalysts were very stable and no obvious loss in photocatalytic efficiency of hydrogen production was observed after five cycles.

© 2016 Elsevier B.V. All rights reserved.

1. Introduction

Photocatalytic water splitting for hydrogen generation is considered as the most promising technology to solve the energy shortage in the future. However, the low quantum yield and light harvesting efficiency of semiconductor photocatalysts for water splitting have limited their practical application. Consequently, many attempts have been made to improve the light energy conversion efficiency of semiconductor photocatalysts, amongst which fabricating porous photocatalysts has been proved to be an efficient strategy. Porous photocatalysts usually have large specific surface areas and abundant catalytically active sites, which could be beneficial to the improvement of light harvesting efficiency and the separation of photogenerated carriers.

Recently, the three-dimensionally ordered macroporous (3DOM) semiconductor materials as photonic crystals have received much attention in photocatalysis field. The periodic structure of 3DOM materials exhibited significant slow photon effect [1–4], which could forbid the propagation of light with certain wavelengths through the material and result in a stop-band reflection. The slow photon effect could increase the path length of light, enhance the photon-matter interaction and further improve the light energy conversion efficiency of semiconductor. A series of 3DOM semiconductor materials, including TiO$_2$ [5–17], Bi$_2$WO$_6$ [18], InVO$_4$ [19–21], WO$_3$ [22,23], BiVO$_4$ [24] and SnO$_2$ [25,26], have been prepared and used as photocatalysts for the decomposition of environmental pollutants. These reported 3DOM semiconductor materials exhibited notably improved photocatalytic activities and showed an attractive prospect in the photocatalysis field. However, only a few of them [27–33] were

used in photocatalytic or photoelectrochemical water splitting for hydrogen generation.

Perovskite strontium titanase (SrTiO$_3$), one of the most promising photocatalysts, has been widely researched for the degradation of various organic contaminants as well as the hydrogen production from water splitting. To improve the light harvesting efficiency of SrTiO$_3$ photocatalyst, several methods have been adopted to fabricate porous SrTiO$_3$ materials with large surface areas. Zou and co-workers synthesized mesoporous SrTiO$_3$ using a sol-gel method [34,35] and a basic molten salt route [36]. Kuang et al. [37] used the layered protonated titanate hierarchical spheres as the template to synthesize single-crystal-like porous SrTiO$_3$ nanocube assemblies. Ouyang et al. [38] synthesized the nanoporous SrTiO$_3$ photocatalysts through a nanotemplate assisted sol-gel hydrothermal reaction. These reported porous SrTiO$_3$ materials exhibited enhanced photocatalytic performance for the photodegradation of organic contaminants and photocatalytic hydrogen evolution from water splitting. However, when the surface area of these nanoporous SrTiO$_3$ photocatalysts increased to a threshold value [36], the light screening effect would hinder the improvement of photocatalytic performance. To develop a SrTiO$_3$ photocatalyst with a 3DOM structure will be helpful to solve this problem due to the slow photon effect of photonic crystals. To the best of our knowledge, however, there is no report focused on 3DOM-SrTiO$_3$.

In this work, the 3DOM-SrTiO$_3$ photonic crystals with different pore sizes were originally fabricated through a colloidal crystal template method and applied as photocatalysts for the hydrogen evolution from water splitting. The effects of Pt loading amount, inverse opal structure and stop-band of 3DOM-SrTiO$_3$ on the catalytic performance were investigated. An amazing increase in hydrogen evolution efficiency was expected over these 3DOM-SrTiO$_3$ photocatalysts due to the slow photon effect of photonic crystals.

2. Experimental

2.1. Materials

Methyl methacrylate (MMA) stabilized with 30 ppm MEHQ, styrene stabilized with 10–15 ppm 4-*tert*-butylcatechol, tetrabutyl titanate [Ti(OBu)$_4$], and chloroplatinic acid hexahydrate (H$_2$PtCl$_6$·6H$_2$O) were purchased from Aladdin. Potassium persulfate (K$_2$S$_2$O$_8$) was obtained from Sinopharm Chemical Reagent Co., Ltd. Acetic acid (CH$_3$COOH) and methanol (CH$_3$OH) were acquired from Concord Technology (Tianjin) Co., Ltd. Strontium nitrate [Sr(NO$_3$)$_2$] and strontium carbonate (SrCO$_3$) were purchased from Tianjin Bodi Chemical Co., Ltd. Citric acid monohydrate (C$_6$H$_8$O$_7$·H$_2$O) was obtained from Tianjin Guangfu Fine Chemical Research Institute. P25 titanium oxide was acquired from Shanghai Macklin Biochemical Co., Ltd. All of the reagents were analytical grade and used as received.

2.2. Characterization

The X-ray powder diffraction (XRD) patterns of the samples were acquired using a Bruker D8 X-ray diffractometer with Cu Kα radiation operated at 40 kV and 40 mA with a scan rate of 0.01° s^{-1} over 2θ range from 5° to 80°. The morphologies of photocatalysts were observed through a JEOL JSM–7500 F field-emission scanning electron microscope (SEM) attached an energy dispersive X-ray spectrometer (EDS). The high-resolution transmission electron microscopy (HRTEM) images were obtained by a Philips Tecnai G2 F20 instrument. Diffuse-reflectance UV–vis (DR UV–vis) spectra were performed on a Shimadzu UV-2550 spectrophotometer in the measurement range from 200 nm to 800 nm N$_2$ sorption analysis

was carried out at 77 K on a Micromeritics TriStar 3000 apparatus and the surface areas were determined by the BET method. The online gas chromatography (GC) analysis was performed on a FL9790II gas chromatograph equipped with a thermal conductive detector (TCD) and a carbon molecular sieve column, using argon as the carrier gas.

2.3. Synthesis of SrTiO$_3$

2.3.1. Synthesis of 3DOM-SrTiO$_3$ with different pore diameters

Polymethylmethacrylate (PMMA) and polystyrene (PS) microspheres with average diameters of 200 nm, 270 nm, and 420 nm were synthesized using a soap-free emulsion polymerization method in the presence of K$_2$S$_2$O$_8$ according to the literature method [39]. The polymer colloidal crystal templates were prepared through a centrifugation method. The detailed synthesis procedure and SEM characterizations of polymer colloidal crystal templates are described in Supplementary materials.

The 3DOM-SrTiO$_3$ materials with different pore sizes were synthesized using the as-synthesized polymer colloidal crystals as templates. The precursor solution of SrTiO$_3$ was prepared as follows. Firstly, 0.01 mol of tetrabutyl titanate was mixed with 10 mL of acetic acid, and then 10 mL of deionized water was added dropwise into the solution with continuous stirring. After that, 0.01 mol of Sr(NO$_3$)$_2$ in 10 mL of deionized water was added dropwise. Finally, 10 mL of 2 mol/L citric acid solution was added. The resulting solution was stirred for another 30 min at room temperature to obtain a clear solution.

The colloidal crystal template was soaked in the precursor solution for 2 h. To remove the redundant precursor solution from the impregnated colloidal crystal template, filtration was carried out. The sample was then dried in a vacuum oven at 50 °C overnight and calcined in a muffle furnace at 650 °C for 4 h to remove the template. The as-synthesized 3DOM-SrTiO$_3$ materials were marked as 3DOM-SrTiO$_3$(200 nm), 3DOM-SrTiO$_3$(270 nm) and 3DOM-SrTiO$_3$(420 nm), respectively, according to the diameter of colloidal crystal template.

2.3.2. Synthesis of disordered macroporous SrTiO$_3$ and solid-state SrTiO$_3$

For comparison, a disordered macroporous SrTiO$_3$ material (denoted as Disorder-SrTiO$_3$) was synthesized through a similar process to that of 3DOM-SrTiO$_3$ materials using the same precursor solution, except that the colloidal crystal template was replaced by a disordered polymer microsphere template.

The solid-state SrTiO$_3$ was synthesized by a solid-state reaction according to the literature [36]. Typically, 0.1 mol of TiO$_2$ (P25) was mixed with an equimolar amount of SrCO$_3$. The mixture was calcined at 900 °C for 5 h. After grinding, it was calcined at 1200 °C for 10 h. The obtained powder sample was denoted as SS-SrTiO$_3$.

2.4. Photocatalytic hydrogen evolution experiments

Photocatalytic hydrogen evolution experiments were carried out over the Pt-loaded photocatalysts and using methanol as a sacrificial reagent under irradiation of 300 W Xe lamp (CEAULIGHT, CEL-HXUV300, 200 nm < λ < 1100 nm, 1100 mW/cm^2). The Pt-loaded photocatalysts were prepared through an in situ photodeposition method. In a typical process, a certain amount of photocatalyst, 150 mL of deionized water, 15 mL of methanol and an appropriate volume of chloroplatinic acid solution (0.0386 mol/L) were added in turn to the reaction vessel. With subsequent stirring, the system was irradiated under a 300 W Xe lamp for 3 h. The obtained Pt-loaded photocatalysts were centrifuged and dried in a vacuum oven at 50 °C overnight.
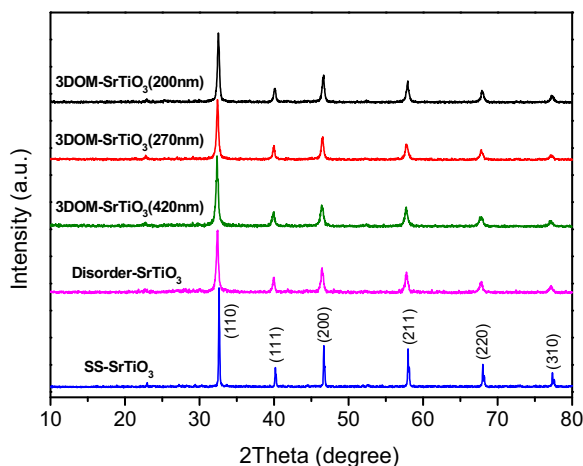
Fig. 1. Powder XRD patterns of 3DOM-SrTiO₃, Disorder-SrTiO₃, and SS-SrTiO₃.

Table 1
The BET surface areas of as-synthesized SrTiO₃ photocatalysts.

Sample	S_{BET} (m² g⁻¹)
3DOM-SrTiO₃(200 nm)	26.4
3DOM-SrTiO₃(270 nm)	23.1
3DOM-SrTiO₃(420 nm)	15.0
Disorder-SrTiO₃	20.3

The photocatalytic hydrogen evolution experiments were performed in a 100 mL quartz flask at room temperature. In a typical process, 0.1 g of Pt-loaded photocatalyst was dispersed in the mixture solution of deionized water (50 mL) and methanol (17 mL) under stirring. The reaction system was thoroughly degassed by evacuation and then irradiated by a 300 W Xe lamp. The evolved hydrogen was analyzed by online GC.

3. Results and discussion

3.1. Characterization of as-synthesized SrTiO₃ materials

The as-synthesized 3DOM-SrTiO₃, Disorder-SrTiO₃, and SS-SrTiO₃ were characterized by XRD, SEM, TEM, DR UV–vis and N₂ sorption.

As shown in Fig. 1, the characteristic diffraction peaks of (110), (111), (200), (211), (220) and (310) can be perfectly indexed to the pure cubic perovskite phase (JCPDS No. 35-0734), and no impurity diffraction peaks were observed in the XRD patterns of all the SrTiO₃ materials. Because of the lower calcination temperature used for 3DOM-SrTiO₃ and Disorder-SrTiO₃, the intensities of the XRD reflections of these two kinds of materials were slightly lower than those of SS-SrTiO₃. The results of XRD characterization indicated that the as-synthesized SrTiO₃ photocatalysts exhibit typical perovskite structure.

The SEM micrographs of 3DOM-SrTiO₃, Disorder-SrTiO₃, and SS-SrTiO₃, at the same magnification, are shown in Fig. 2a–e (more SEM micrographs of 3DOM-SrTiO₃ materials at different magnifications are shown in Fig. S2 of Supplementary materials). It could be clearly demonstrated that all the as-synthesized 3DOM-SrTiO₃ materials possessed well-ordered inverse opal structures. The average pore diameters of 3DOM-SrTiO₃(200 nm), 3DOM-SrTiO₃(270 nm) and 3DOM-SrTiO₃(420 nm) were about 110 nm, 150 nm and 230 nm, respectively, which showed a shrinkage of ~45% compared with the polymer microspheres. Disorder-SrTiO₃ exhibited the porous structure derived from the disordered accumulation of SrTiO₃ nanoparticles. While, SS-SrTiO₃ was made up of micron-sized particles. The EDS spectrum of 3DOM-SrTiO₃(270 nm) is shown in Fig. 2f, which indicated that the 3DOM-SrTiO₃(270 nm) materials were composed of Sr, Ti, and O elements and the atomic ratio of Sr/Ti is ca. 1:1. The EDS characterization results further confirmed the successful fabrication of SrTiO₃ with typical perovskite structure.

The morphology and pore diameter of as-synthesized 3DOM-SrTiO₃ were characterized by TEM. Fig. 3 describes the TEM images of 3DOM-SrTiO₃(270 nm). It could be found that 3DOM-SrTiO₃(270 nm) exhibited a typical well-ordered inverse opal

structure. In addition, the pore diameter determined from TEM was well consistent with the results of SEM characterization.

Fig. 4 depicts the DR UV–vis spectra of 3DOM-SrTiO₃, Disorder-SrTiO₃, and SS-SrTiO₃. The band gap energies of these photocatalysts were estimated from the $(\alpha h\nu)^2$–$h\nu$ plots. It could be found that the band gap energies of 3DOM-SrTiO₃ and Disorder-SrTiO₃ were about 3.3 eV. While the band gap energy of SS-SrTiO₃ was 3.2 eV, which was similar to the reported result [36,37,40]. The slight blueshift of the optical absorption edge of 3DOM-SrTiO₃ compared with SS-SrTiO₃ could be attributed to the quantum size effect, which means that the energy level changes from quasi-continuous to discrete when the particle size decreases [36].

The BET surface areas of the obtained 3DOM-SrTiO₃ and Disorder-SrTiO₃ photocatalysts are listed in Table 1. It could be found that the BET surface areas of 3DOM-SrTiO₃ and Disorder-SrTiO₃ were in the range of 15.0–26.4 m² g⁻¹. With the decrease of pore size, BET surface areas of 3DOM-SrTiO₃ gradually increased from 15.0 m² g⁻¹ for 3DOM-SrTiO₃(420 nm) to 26.4 m² g⁻¹ for 3DOM-SrTiO₃(200 nm). Disorder-SrTiO₃ exhibited medium-level BET surface area (20.3 m² g⁻¹) compared with 3DOM-SrTiO₃ photocatalysts due to the unconsolidated porous structure.

3.2. Effect of Pt loading amount on the efficiency of photocatalytic hydrogen production

The Pt nanoparticles were employed as co-catalysts in this work through a photodeposition method. The influence of Pt loading amount on the efficiency of photocatalytic hydrogen production over 3DOM-SrTiO₃ was investigated. For the catalysts of 3DOM-SrTiO₃(200 nm) and 3DOM-SrTiO₃(270 nm), as shown in Fig. 5, the highest efficiencies of hydrogen evolution were obtained when the Pt loading amount was 0.7 wt%. While 3DOM-SrTiO₃(420 nm) afforded the highest catalytic activity as the Pt loading amount was 0.5 wt%, which could be attributed to the lower surface area of 3DOM-SrTiO₃(420 nm) compared with 3DOM-SrTiO₃(200 nm) and 3DOM-SrTiO₃(270 nm). Further increasing the Pt loading amount, the efficiency of hydrogen evolution decreased significantly, which could be explained by the fact that the excess Pt nanoparticles may promote the recombination of the photogenerated electrons and holes. Taking into account that the highest efficiency of hydrogen production was obtained over 3DOM-SrTiO₃(270 nm) with Pt loading of 0.7 wt%, the optimum Pt loading amount on 3DOM-SrTiO₃ catalysts in this work was considered as 0.7 wt%.

3.3. Effect of inverse opal structure on the efficiency of photocatalytic hydrogen production

The influence of inverse opal structure on the photocatalytic performance of 3DOM-SrTiO₃ was investigated in this section. Fig. 6 describes the efficiencies of hydrogen evolution from water splitting over 3DOM-SrTiO₃, Disorder-SrTiO₃, and SS-SrTiO₃. The hydrogen evolution rate over SS-SrTiO₃ was 114 μmol/g h, which was comparable to the results in the literature [36] under similar reaction conditions. Disorder-SrTiO₃ exhibited increased efficiency of hydrogen evolution (326 μmol/g h) compared with SS-SrTiO₃. This could be attributed to the larger surface area of Disorder-SrTiO₃ that could provide more active sites, as well as its nanosized
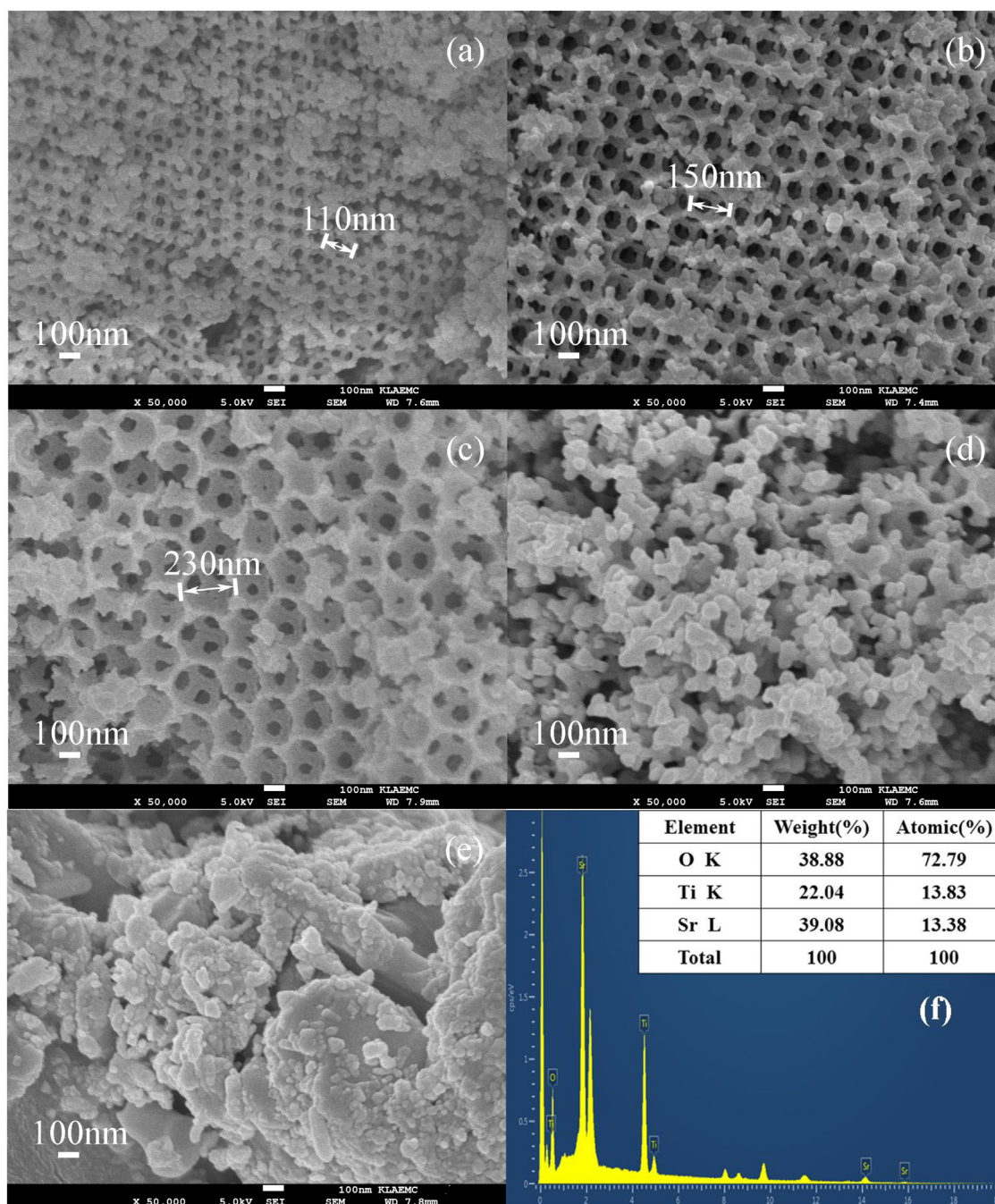
Fig. 2. SEM micrographs of (a) 3DOM-SrTiO$_3$(200 nm), (b) 3DOM-SrTiO$_3$(270 nm), (c) 3DOM-SrTiO$_3$(420 nm), (d) Disorder-SrTiO$_3$, (e) SS-SrTiO$_3$, and EDS spectrum of (f) 3DOM-SrTiO$_3$(270 nm).

pore wall that could decrease the recombination of photogenerated electrons and holes.

To our delight, 3DOM-SrTiO$_3$ exhibited significant improvement in photocatalytic hydrogen evolution efficiency compared with Disorder-SrTiO$_3$ and SS-SrTiO$_3$. Among all the synthesized 3DOM-SrTiO$_3$ photocatalysts, 3DOM-SrTiO$_3$(270 nm) performed best in the photocatalytic water splitting reaction for hydrogen production. The highest efficiency of hydrogen evolution reached 3599 μmol/g h, which was 31 times as high as that of SS-SrTiO$_3$. To the best of our knowledge, this is the highest result for the similar reaction system over SrTiO$_3$ photocatalysts [36,37,40] (the detailed comparison was described in Supplementary materials). Moreover, the efficiencies of hydrogen production over 3DOM-SrTiO$_3$(200 nm) and 3DOM-SrTiO$_3$(420 nm) were 1817 μmol/g h and 936 μmol/g h, respectively, which were also notably higher than SS-SrTiO$_3$ and Disorder-SrTiO$_3$. This meant that the three-dimensionally ordered macroporous structure of 3DOM-SrTiO$_3$ could remarkably improve the photocatalytic performance in water splitting, which may be explained by the following reasons. Firstly, the larger surface area of 3DOM-SrTiO$_3$ could provide more active sites on the surface of photocatalysts. Secondly, the nanosized wall of 3DOM-SrTiO$_3$ could shorten the diffusion length of photogenerated electron-hole pairs and thus prevent their recombination. Finally and most importantly, the slow photon effect of 3DOM-SrTiO$_3$ could obviously increase the photon-matter interaction
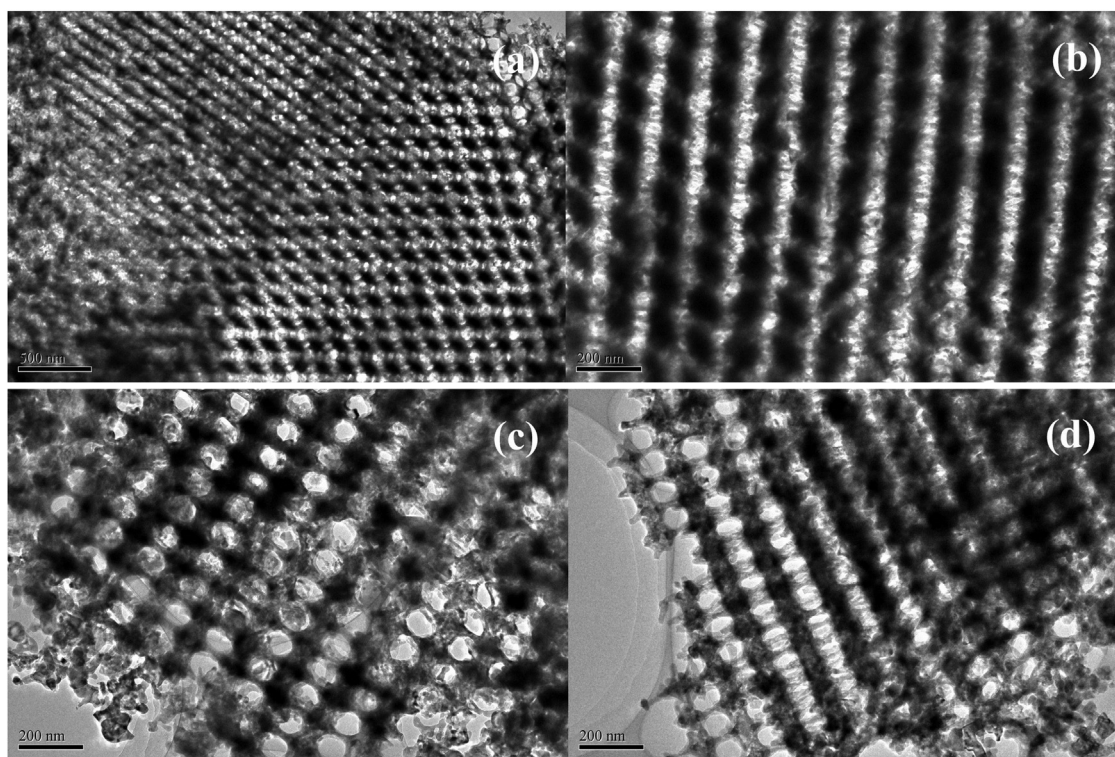
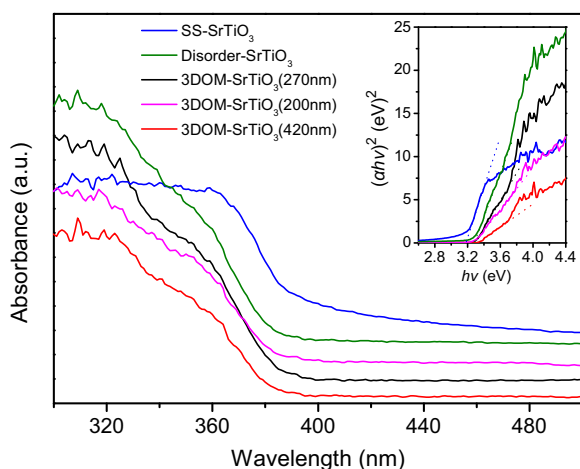**Fig. 3.** TEM images of 3DOM-SrTiO$_3$(270 nm) photocatalyst.

Fig. 4. DR UV–vis spectra and $(\alpha h\nu)^2$–$h\nu$ plots (inset) of 3DOM-SrTiO$_3$, Disorder-SrTiO$_3$, and SS-SrTiO$_3$ photocatalysts.

Fig. 5. The efficiencies of hydrogen evolution over 3DOM-SrTiO$_3$ with different Pt loadings.

length and consequently enhance the light energy conversion efficiency.

3.4. Effect of 3DOM-SrTiO$_3$ stop-band on the efficiency of photocatalytic hydrogen production

In order to investigate the influence of stop-band on the photocatalytic performance of 3DOM-SrTiO$_3$, the stop-bands of 3DOM-SrTiO$_3$ materials were calculated through the modified Bragg's law (as described in Equation (1))[23,41]. In this equation, $\lambda_{\max}$ is the wavelength of stop-band, D is the pore diameter of 3DOM-SrTiO$_3$, n_{SrTiO3} and n_{Water} are the refractive index of SrTiO$_3$ and water, respectively, f is the SrTiO$_3$ phase volume percentage (for an fcc structure, generally $f = 0.26$), and θ is the incident angle of light. Because these 3DOM-SrTiO$_3$ powder samples were directly
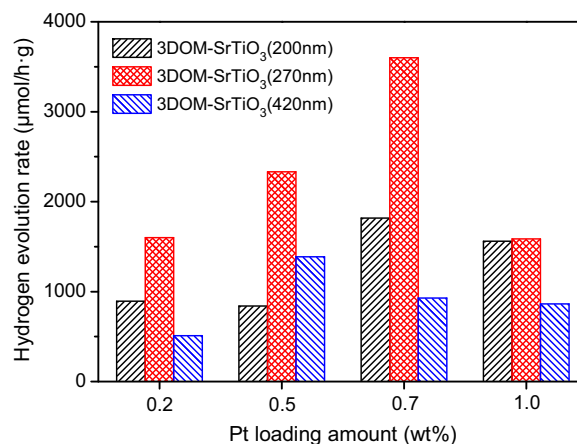
suspended in reaction solution, the incident angle of light irradiation to the photocatalysts should be varied over a wide range from 0° to 90°. Therefore, the calculated stop-bands of 3DOM-SrTiO$_3$(200 nm) ($D = 110$ nm), 3DOM-SrTiO$_3$(270 nm) ($D = 150$ nm), and 3DOM-SrTiO$_3$(420 nm) ($D = 230$ nm) were in the ranges of $243 \sim 302$ nm, $331 \sim 412$ nm, and $507 \sim 631$ nm, respectively. That is to say, the lights with wavelength in these ranges are more likely to be reflected into the macropores of 3DOM-SrTiO$_3$, leading to the enhancement of photon-matter interaction.

$$\lambda_{\max} = 2\sqrt{\frac{2}{3}}D\sqrt{n_{SrTiO3}^2 f + n_{water}^2(1-f) - \sin^2\theta} \qquad (1)$$

It could be found from Fig. 4 that the optical absorption edge of 3DOM-SrTiO$_3$ materials was estimated to be ∼380 nm. The electronic absorption band of SrTiO$_3$ was exactly overlapped with the
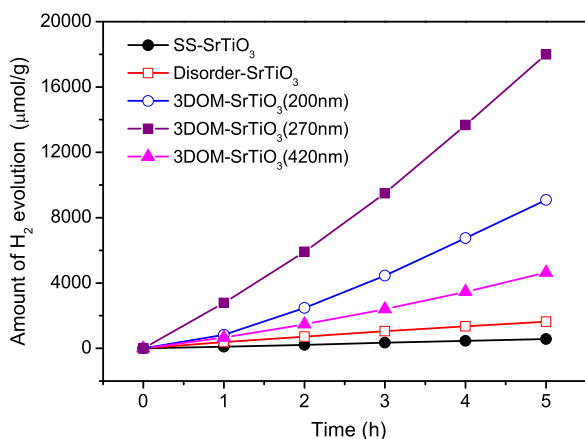
Fig. 6. The efficiencies of hydrogen evolution over 3DOM-SrTiO₃, Disorder-SrTiO₃, and SS-SrTiO₃.

Fig. 8. Cycling tests of 3DOM-SrTiO₃(270 nm) for hydrogen production from photocatalytic water splitting.
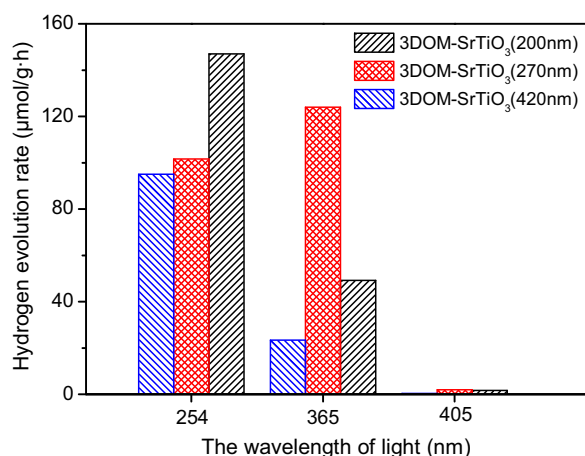

Fig. 7. The efficiencies of hydrogen evolution over 3DOM-SrTiO₃ under the certain wavelength light irradiation.

stop-band of 3DOM-SrTiO₃(270 nm), which exhibited the highest catalytic performance for water splitting. Thus it is logical to deduce that the slow photon effect of 3DOM-SrTiO₃ could significantly improve the photocatalytic performance when the photonic stop-band of 3DOM-SrTiO₃ was overlapped with the electronic absorption band of SrTiO₃.

To further confirm the influence of 3DOM-SrTiO₃ stop-band on hydrogen evolution efficiency, the photocatalytic water splitting experiments under the certain wavelength light irradiation (300 W Xe lamp equipped with a short-wavelength pass filter of 254 nm, 365 nm, or 405 nm) were carried out over 3DOM-SrTiO₃ catalysts. Fig. 7 shows the efficiencies of hydrogen evolution in these controlled experiments over 3DOM-SrTiO₃(200 nm), 3DOM-SrTiO₃(270 nm) and 3DOM-SrTiO₃(420 nm). It could be clearly seen that 3DOM-SrTiO₃(200 nm) exhibited the highest photocatalytic performance in water splitting under irradiation of 254 nm light, which could be attributed to the proper stop-band of 3DOM-SrTiO₃(200 nm). In addition, 3DOM-SrTiO₃(270 nm) performed best under irradiation of 365 nm light compared with 3DOM-SrTiO₃(200 nm) and 3DOM-SrTiO₃(420 nm) for the same reason. This is a direct experimental evidence for the influence of stop-band of 3DOM-SrTiO₃. When the wavelength of incident light increased to 405 nm, the efficiencies of hydrogen evolution over these 3DOM-SrTiO₃ photocatalysts notably decreased because of the wide band gap of SrTiO₃ materials. It was also in accordance with the results of DR UV–vis characterization. The results of these
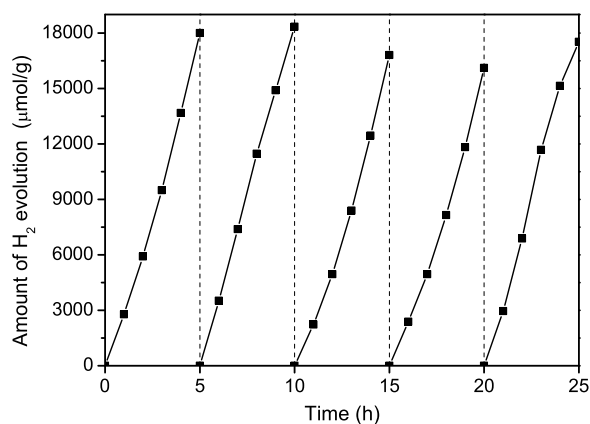
controlled water splitting experiments further confirmed the conclusion that the significantly improved photocatalytic performance of 3DOM-SrTiO₃(270 nm) could be attributed to the exact overlap of photonic stop-band and electronic absorption band of 3DOM-SrTiO₃.

3.5. Photocatalytic stability of the 3DOM-SrTiO₃ photocatalyst

To investigate the photocatalytic stability of 3DOM-SrTiO₃ photocatalysts, 3DOM-SrTiO₃(270 nm) was employed as a model catalyst in a cycling water splitting experiment. After 5 h irradiation, the reaction system was thoroughly degassed by evacuation to remove produced hydrogen. Fig. 8 shows the efficiencies of hydrogen evolution over 3DOM-SrTiO₃(270 nm) for five cycling tests. It could be found that the hydrogen evolution rate still remained more than 3500 μmol/g·h after five cycles. The results indicated that the obtained 3DOM-SrTiO₃ photocatalysts exhibited excellent durability in water splitting experiment and no obvious decrease in catalytic performance was observed after five cycles.

4. Conclusions

In summary, the novel 3DOM-SrTiO₃ photonic crystal photocatalysts were synthesized and applied in the water splitting for hydrogen production. The results of XRD, SEM and TEM characterizations clearly demonstrated that as-synthesized 3DOM-SrTiO₃ materials possessed typical perovskite structure and well-ordered inverse opal structure. The effects of Pt loading amount, inverse opal structure and stop-band of 3DOM-SrTiO₃ on the efficiency of photocatalytic hydrogen production were investigated. 3DOM-SrTiO₃ photocatalysts exhibited significantly improved photocatalytic performance in water splitting compared with SS-SrTiO₃ and Disorder-SrTiO₃. Among these obtained 3DOM-SrTiO₃ catalysts, 3DOM-SrTiO₃(270 nm) with a Pt loading of 0.7 wt% showed a highest hydrogen evolution rate of 3599 μmol/g·h, which was 31 times as high as that of SS-SrTiO₃ and 11 times higher than that of Disorder-SrTiO₃. To the best of our knowledge, this is the highest result for the similar reaction systems over SrTiO₃ photocatalysts. The notably increased photocatalytic efficiency of hydrogen evolution could be attributed to the exact overlap between the stop-band of 3DOM-SrTiO₃(270 nm) and the band gap of SrTiO₃. Furthermore, 3DOM-SrTiO₃(270 nm) was very stable and the hydrogen production rate still remained more than 3500 μmol/g h after five cycles.

Acknowledgements

Appendix A. Supplementary data

Supplementary data associated with this article can be found, in the online version, at http://dx.doi.org/10.1016/j.apcatb.2016.07.049.

References

[1] M. Srinivasarao, D. Collings, A. Philips, S. Patel, Science 292 (2001) 79–83.
[2] A. Stein, B.E. Wilson, S.G. Rudisill, Chem. Soc. Rev. 42 (2013) 2763–2803.
[3] Y. Wei, J. Jiao, Z. Zhao, J. Liu, J. Li, G. Jiang, Y. Wang, A. Duan, Appl. Catal. B: Environ. 179 (2015) 422–432.
[4] M. Curti, J. Schneider, D.W. Bahnemann, C.B. Mendive, J. Phys. Chem. Lett. 6 (2015) 3903–3910.
[5] S. Nishimura, N. Abrams, B.A. Lewis, L.I. Halaoui, T.E. Mallouk, K.D. Benkstein, J. van de Lagemaat, A.J. Frank, J. Am. Chem. Soc. 125 (2003) 6306–6310.
[6] S.-H.A. Lee, N.M. Abrams, P.G. Hoertz, G.D. Barber, L.I. Halaoui, T.E. Mallouk, J. Phys. Chem. B 112 (2008) 14415–14421.
[7] Y. Li, F. Piret, T. Léonard, B.-L. Su, J. Colloid Interface Sci. 348 (2010) 43–48.
[8] M. Wu, Y. Li, Z. Deng, B.-L. Su, ChemSusChem 4 (2011) 1481–1488.
[9] M. Wu, A. Zheng, F. Deng, B.-L. Su, Appl. Catal. B: Environ. 138–139 (2013) 219–228.
[10] D. Qi, L. Lu, Z. Xi, L. Wang, J. Zhang, Appl. Catal. B: Environ. 160–161 (2014) 621–628.
[11] J.I.L. Chen, G. von Freymann, S.Y. Choi, V. Kitaev, G.A. Ozin, Adv. Mater. 18 (2006) 1915–1919.
[12] M. Srinivasan, T. White, Environ. Sci. Technol. 41 (2007) 4405–4409.
[13] Q. Li, J.K. Shang, J. Am. Ceram. Soc. 91 (2008) 660–663.
[14] J.I.L. Chen, G.A. Ozin, J. Mater. Chem. 19 (2009) 2675–2678.
[15] J. Xu, B. Yang, M. Wu, Z. Fu, Y. Lv, Y. Zhao, J. Phys. Chem. C 114 (2010) 15251–15259.
[16] F. Sordello, C. Duca, V. Maurino, C. Minero, Chem. Commun. 47 (2011) 6147–6149.
[17] Y. Lu, H. Yu, S. Chen, X. Quan, H. Zhao, Environ. Sci. Technol. 46 (2012) 1724–1730.
[18] S. Sun, W. Wang, L. Zhang, J. Mater. Chem. 22 (2012) 19244–19249.
[19] Y. Wang, H. Dai, J. Deng, Y. Liu, H. Arandiyan, X. Li, B. Gao, S. Xie, Solid State Sci. 24 (2013) 62–70.
[20] Y. Wang, H. Dai, J. Deng, Y. Liu, Z. Zhao, X. Li, H. Arandiyan, Chem. Eng. J. 226 (2013) 87–94.
[21] K. Ji, J. Deng, H. Zang, J. Han, H. Arandiyan, H. Dai, Appl. Catal. B: Environ. 165 (2015) 285–295.
[22] M. Sadakane, K. Sasaki, H. Kunioku, B. Ohtani, R. Abe, W. Ueda, J. Mater. Chem. 20 (2010) 1811–1818.
[23] X. Chen, J. Ye, S. Ouyang, T. Kako, Z. Li, Z. Zou, ACS Nano 5 (2011) 4310–4318.
[24] K. Ji, H. Dai, J. Deng, H. Zang, H. Arandiyan, S. Xie, H. Yang, Appl. Catal. B: Environ. 168–169 (2015) 274–282.
[25] S.-L. Chen, A.-J. Wang, C. Dai, J.B. Benziger, X.-C. Liu, Chem. Eng. J. 249 (2014) 48–53.
[26] L. Chen, L. Xie, M. Wang, X. Ge, J. Mater. Chem. A 3 (2015) 2991–2998.
[27] L.N. Quan, Y.H. Jang, K.A. Stoerzinger, K.J. May, Y.J. Jang, S.T. Kochuveedu, Y. Shao-Horn, D.H. Kim, Phys. Chem. Chem. Phys. 16 (2014) 9023–9030.
[28] K.Y. Yoon, J.S. Lee, K. Kim, C.H. Bak, S.I. Kim, J.B. Kim, J.H. Jang, ACS Appl. Mater. Interfaces 6 (2014) 22634–22639.
[29] L. Zhang, C.-Y. Lin, V.K. Valev, E. Reisner, U. Steiner, J.J. Baumberg, Small 10 (2014) 3970–3978.
[30] X. Zhang, Y. Liu, S.-T. Lee, S. Yang, Z. Kang, Energy Environ. Sci. 7 (2014) 1409–1419.
[31] Z. Zhang, X. Yang, M.N. Hedhili, E. Ahmed, L. Shi, P. Wang, ACS Appl. Mater. Interfaces 6 (2014) 691–696.
[32] M. Zhou, J. Bao, Y. Xu, J. Zhang, J. Xie, M. Guan, C. Wang, L. Wen, Y. Lei, Y. Xie, ACS Nano 8 (2014) 7088–7098.
[33] F. Sordello, C. Minero, Appl. Catal. B: Environ. 163 (2015) 452–458.
[34] X. Fan, Y. Wang, X. Chen, L. Gao, W. Luo, Y. Yuan, Z. Li, T. Yu, J. Zhu, Z. Zou, Chem. Mater. 22 (2010) 1276–1278.
[35] H. Yu, S. Ouyang, S. Yan, Z. Li, T. Yu, Z. Zou, J. Mater. Chem. 21 (2011) 11347–11351.
[36] H. Liu, X. Chen, S. Yan, Z. Li, Z. Zou, Eur. J. Inorg. Chem. 2014 (2014) 3731–3735.
[37] Q. Kuang, S. Yang, ACS Appl. Mater. Interfaces 5 (2013) 3683–3690.
[38] S. Ouyang, P. Li, H. Xu, H. Tong, L. Liu, J. Ye, ACS Appl. Mater. Interfaces 6 (2014) 22726–22732.
[39] Y. Chang, K. Yu, C. Zhang, R. Li, P. Zhao, L.-L. Lou, S. Liu, Appl. Catal. B: Environ. 176–177 (2015) 363–373.
[40] H. Tan, Z. Zhao, W.-b. Zhu, E.N. Coker, B. Li, M. Zheng, W. Yu, H. Fan, Z. Sun, ACS appl, Mater. Interfaces 6 (2014) 19184–19190.
[41] M. Ren, R. Ravikrishna, K.T. Valsaraj, Environ. Sci. Technol. 40 (2006) 7029–7033.